Author Manuscript

Author Manuscript

Author Manuscript

Author Manuscript

HHS Public Access

Author manuscript

*Biomaterials*. Author manuscript; available in PMC 2019 October 01.

Published in final edited form as:

*Biomaterials*. 2018 October ; 179: 71–82. doi:10.1016/j.biomaterials.2018.06.030.

# Studying biomineralization pathways in a 3D culture model of breast cancer microcalcifications

**Netta Vidavsky**[1], **Jennie AMR Kunitake**[1], **Aaron E Chiou**[2], **Paul A Northrup**[3], **Teresa Porri**[4], **Lu Ling**[2], **Claudia Fischbach**[2,5,*], **Lara A Estroff**[1,5,*]

[1]Department of Materials Science and Engineering, Cornell University, Ithaca, NY

[2]Nancy E. and Peter C. Meinig School of Biomedical Engineering, Cornell University, Ithaca, NY

[3]National Synchrotron Light Source II, Brookhaven National Laboratory, Upton, NY

[4]Institute of Biotechnology, Cornell University, Ithaca, NY

[5]Kavli Institute at Cornell for Nanoscale Science, Ithaca, NY

## Abstract

Microcalcifications serve as diagnostic markers for breast cancer, yet their formation pathway(s) and role in cancer progression are debated due in part to a lack of relevant 3D culture models that allow studying the extent of cellular regulation over mineralization. Previous studies have suggested processes ranging from dystrophic mineralization associated with cell death to bone-like mineral deposition. Here, we evaluated microcalcification formation in 3D multicellular spheroids, generated from non-malignant, pre-cancer, and invasive cell lines from the MCF10A human breast tumor progression series. The spheroids with greater malignancy potential developed necrotic cores, thus recapitulating spatially distinct viable and non-viable areas known to regulate cellular behavior in tumors *in vivo*. The spatial distribution of the microcalcifications, as well as their compositions, were characterized using nanoCT, electron-microscopy, and X-ray spectroscopy. Apatite microcalcifications were primarily detected within the viable cell regions and their number and size increased with malignancy potential of the spheroids. Levels of alkaline phosphatase decreased with malignancy potential, whereas levels of osteopontin increased. These findings support a mineralization pathway in which cancer cells induce mineralization in a manner that is linked to their malignancy potential, but that is distinct from physiological osteogenic mineralization.

### Keywords

Pathological mineralization; Multicellular spheroids; Ductal carcinoma in situ; XANES

*Corresponding authors.

Author contributions: N.V, C.F. and L.E. conceived and designed the study. N.V. performed experiments in assistance with J.K., A.C., L.L., P.N., and T.P. N.V, J.K., A.C, P.N, C.F. and L.E. discussed the experiments and results. J.K. made graphical scheme. N.V. wrote the initial draft. C.F. and L.E revised the final draft with assistance of all co-authors. All authors have approved the final article.

Competing financial interests

The authors declare no competing financial interests.

Author Manuscript Author Manuscript Author Manuscript Author Manuscript

## Introduction

Breast cancer screening, e.g., mammography, frequently relies on microcalcifications (MCs), and their chemical composition, e.g., calcium phosphate, most commonly non-stoichiometric apatite, versus calcium oxalate, is associated with tumor malignancy[1–4]. Little is known, however, about how they form in the body and their role in cancer progression. MCs are an example of a broader class of pathological mineral deposits, in which mineral formation occurs in tissues that normally do not mineralize[5–11]. Based upon our understanding of biomineralization, multiple pathways have been suggested for how pathological mineral deposits form[12], ranging from unregulated mineralization in necrotic areas to regulated mineralization, which is similar to physiological bone mineralization[13]. In the specific case of MC formation in breast tumors, a key question is how are cancer cells involved in the mineralization process? In order to address this question, we aimed to develop an *in vitro* breast tumor model to study the extent of cellular regulation in MC formation as a function of malignancy potential.

Pathological mineral formation can follow cellularly ‘unregulated’, ‘regulated’ and ‘dysregulated’ pathways. Often MCs are observed in necrotic areas of human breast tumors and are most likely the result of unregulated mineralization[14,15]. Unregulated mineralization occurs in areas of cell death and most likely results from some combination of abnormal homeostasis in injured or necrotic cells, local increases in calcium and phosphate concentrations, and apatite nucleation on cellular debris[16–18]. MCs in breast lesions are also thought to be associated with viable cancer cells undergoing epithelial to mesenchymal transition (EMT)[3] and with increased expression of bone matrix proteins such as osteopontin (OPN)[19–21]. Based on this evidence, it has been suggested that MCs form through regulated physiological, or bone-like mineralization[3,22], in which epithelial cancer cells undergo osteogenic differentiation to resemble osteoblasts, the mesenchymal bone-forming cells. It is also possible, however, that the viable cells have a role in a third pathway, dysregulated mineralization, in which the balance between mineralization inhibitors and promotors is skewed away from the normal balance. For example, when Matrix GLA protein or fetuin A, known mineralization inhibitors, are knocked-out in mouse models, mineral deposition is observed in multiple soft tissues due to a disruption of the normal cellular regulation of mineralization[6,23].

Currently, the primary *in vitro* model to study MC formation uses breast epithelial cell lines cultured on polystyrene surfaces in osteogenic media (addition of β-glycerolphosphate and ascorbic acid)[24,25]. Results obtained using this 2D culture model suggest that cells regulate MC formation in a similar manner to bone formation[24,25], however the use of osteogenic media biases the system towards mineralization through upregulation of alkaline phosphatase (ALP) and osteogenic differentiation[26–28]. In addition, culture on plastic surfaces fails to recapitulate key aspects of the breast tumor microenvironment including 3D cell-cell and cell-extracellular matrix (ECM) interactions as well as varied diffusion/reaction processes influencing the formation of clearly separated necrotic and viable cell regions[29,30]. For these reasons, 3D tumor models are becoming prevalent in cancer research and may be suitable to study the formation of MCs under conditions that are more pathologically relevant than 2D cultures[31,32]. In particular, mammary multicellular

Author Manuscript Author Manuscript Author Manuscript Author Manuscript

spheroids form when breast epithelial cells are cultured in a non-adhesive environment[33,34]. Under these conditions, the cells aggregate into 3D structures with morphological features of acini. Much like tumors, multicellular spheroids develop necrosis at their core as their size exceeds the diffusion limit of oxygen and nutrients, while at their periphery cells continue to proliferate and function, providing a system with discrete areas of viable cells in the periphery and a core of dead cells.

While multiple breast epithelial cell lines are available, the MCF10A human breast tumor progression series provides a family of isogenic cell lines with increasing malignancy potential. The parent MCF10A cell line[35] represents benign human breast epithelial cells and was initially isolated from a woman with fibrocystic disease. The cell lines MCF10DCIS.com[36,37] and MCF10CA1a[38] were derived from MCF10A through Ras-transformation and subsequent xenograft passaging in immune deficient mice, and possess characteristics of DCIS and invasive tumors, respectively. While MCF10A cells are incapable of forming tumors in mice, DCIS.com cells will form comedo DCIS when xenografted into mice and MCF10CA1a cells will always form tumors, hence they are considered to be of increasing malignancy potential. Together, these three cell lines allow modeling varying stages of breast cancer ranging from non-malignant, through DCIS (pre-cancerous) to invasive and provide an opportunity to investigate the effect of cell phenotype on MC formation.

Here, we study MC formation pathways, as a function of tumor cell malignancy potential, using a 3D spheroid model of breast cancer consisting of cells from the MCF10A tumor progression series. In contrast to previous 2D studies, we avoid introducing any osteogenic agents, which are known to induce mineralization, as there is currently no evidence suggesting that breast cancer cells are exposed to an osteogenic environment *in vivo*. To identify MCs within the 3D spheroids, we employ a series of high resolution imaging and spectroscopy techniques that enable detection of particles in the size range of clinically relevant MCs (~1 μm) within an organic matrix.

## Materials and Methods

### Cell culture.

A series of immortalized human breast epithelial cells including normal MCF10A (ATCC), malignant MCF10DCIS.com and MCF10CA1a (both from Karmanos Cancer Institute) were used. Cells were cultured in enriched DMEM/F12 media (1% Penicillin/Streptomycin, 5% horse serum, 10 mg/mL insulin, 0.5 mg/mL hydrocortisone, 100 ng/mL choleratoxin, 20 ng/mL EGF) and in calcium and magnesium serum level enriched DMEM/F12. In the serum-level media $CaCl_2$ and $MgSO_4 \cdot 10H_2O$ were added to enriched DMEM/F12 media to achieve final concentration of 2.2 mM calcium and 0.8 mM magnesium. The cells were cultured at 37°C and 5% $CO_2$ with refreshing media every 48 h. All quantitative experiments were carried out in triplicate or higher and all experiments were independently repeated at least twice. Data are expressed as mean ± standard deviation.

Author Manuscript Author Manuscript Author Manuscript Author Manuscript

### Spheroid formation.

96-well plates were used for spheroid culture under sterile conditions. The bottom of each well was coated with 50 μL of 1.5% low melt agarose in DMEM/F12 (50°C), to prevent cell adhesion[33]. Cells of 80% confluency were trypsinized and seeded at a density of 5000 cells/100 μL DMEM/F12 into each well (Day 0). The 96-well plates were incubated at 37°C and 5% $CO_2$ on a shaker, to encourage cell-cell adhesion in suspension and consequential spheroid formation. On Day 1, 100 μL of enriched DMEM/F12 media with $CaCl_2$ and $MgSO_4 \cdot 10H_2O$ were added to obtain media concentration of 2.2 mM Ca and 0.8 mM Mg. 100 μL media were aspirated and fresh 100 μL media were added every 48 h.

### Human breast tissue sample.

A de-identified ductal carcinoma *in situ* (DCIS) tissue sample was generously provided by Dr. Cliff Hudis (Memorial Sloan Kettering Cancer Center) where it was collected under approval from the Institutional Review Board. The tissue was snap frozen immediately after surgical removal via mastectomy, embedded in optimal cutting temperature compound (OCT) and maintained at −80°C. The tissue was sectioned (12 μm thickness) on a microtome (Thermo Scientific HM550 Cryostat), and the section was mounted onto slides (Fisherbrand® Superfrost®/Plus microscope slides). Hematoxylin and eosin (H&E) staining was carried out at the Cornell College of Veterinary Medicine Animal Health Diagnostic Center using standard protocols. The stained section was then taken to the Department of Pathology and Laboratory Medicine at Cayuga Medical Center (Ithaca, NY) for pathological analysis and the region indicated (Fig. 1f) determined to be DCIS.

### 2D culture and analysis.

Cells were seeded into 6-well plates at a density of $1.5 \times 10^5$ cells per well in 2 mL enriched DMEM/F12. After 48 hours, the media was aspirated and fresh DMEM/F12 media supplemented with 2.2 mM Ca and 0.8 mM Mg was added, and changed every 48 hours. After 10 days of culture the cells were fixed with 1 mL 10% formalin. After fixation, the wells were washed with DI water three times and stained with von Kossa or Alizarin Red stain. For **von Kossa staining**, for each well, 1 mL of silver nitrate (5%) was applied for 1 h under a UV lamp, followed by three washes with DI water and sodium thiosulphate (5%) treatment for 2 minutes and three washes with DI water. For **alizarin Red staining (ARS)**, 40 mM ARS solution was prepared by dissolving 0.685 g ARS into 50 mL DI water and adjusting the pH to 4.1 by using 10% ammonium hydroxide. For each well, 1 mL of 40 mM ARS solution was added and kept in room temperature for 20 minutes. The dye was aspirated and washed with 2 mL DI water for 5 minutes.

### Spheroid preparation for sectioning and histology.

10–25 spheroids were collected into a 1.5 mL centrifuge tube and fixed with 4% paraformaldehyde for 30 minutes. Following washes with PBS spheroids were stained with either Methylene blue or Eosin Y to enable localization during histological processing. 5–10 fixed spheroids were placed in Tissue-Tek biopsy cryomolds (Sakura) and the remaining PBS was aspirated. Optical cutting media (OCT) was added and the molds were quickly placed in liquid nitrogen and in −20°C before cutting. Cryo-sectioning was carried out using

Author Manuscript Author Manuscript Author Manuscript Author Manuscript

a cryo microtome (Thermo Scientific HM550 Cryostat). 20 μm-thick sections were mounted on fused quartz slides (Electron Microscopy Sciences) and air dried before SEM imaging. 20 μm-thick sections were mounted on Kapton tape (Saint-Gobain) for XRF and XANES analyses. For preparation of paraffin cross-sections, 10–20 fixed spheroids were placed in Tissue-Tek biopsy cryomolds (Sakura). Warm 2% low melt agarose solution in DI water was added and left to solidify for 10 minutes at room temperature. The cryomolds were put on ice for 1 minute, and the gel cube was taken out of the mold, wrapped in a Surgipath biowrap (Leica Microsystems), put inside a multichamber biopsy cassette and stored in 70% Ethanol. Spheroids in the cassettes were dehydrated, paraffin embedded, sectioned to a thickness of 5 micrometers and stained with hematoxylin and eosin (H&E) and von Kossa/Nuclear Fast Red at the Cornell College of Veterinary Medicine Animal Health Diagnostic Center using standard protocols. A minimum of 5 spheroid sections was analyzed for each cell-type.

### Immunohistochemistry.

Paraffin-sections of the spheroids were stained using the VECTASTAIN Elite ABC Kit (Vector Laboratories) and a minimum of 4 spheroid sections for each cell type (1 section each from 4 spheroids) was analyzed. Briefly, sections were deparaffinized in xylene and rehydrated before heat-based antigen retrieval in 10 mM citrate buffer, pH 6 for 20 min at 95°C. Endogenous peroxidase activity was quenched with 3% hydrogen peroxide for 30 min. Sections were blocked with normal horse serum for 30 min. Next, sections were incubated with primary antibodies against osteopontin (OPN; EMD Millipore, AB 1870, diluted 1:750) and alkaline phosphatase (ALP; Abcam, ab108337, diluted 1:500) overnight at 4°C. Sections were incubated with biotinylated horse anti-mouse/rabbit IgG for 1 h, then with avidin-biotinylated peroxidase complex for 30 min. Stain was developed in diaminobenzidine (DAB; Thermo Scientific) solution for 3 min. Nuclei were counterstained using Mayer's hematoxylin (Thermo Scientific) for 20 s and then sections were dehydrated and mounted with Entellan (EMD Millipore). Sections were imaged using a Scanscope® CS0 (Aperio, Vista, CA) with 40x objective. For IHC quantitative analysis, Aperio ImageScope v12.1.0.5029 software was used. For each condition, sections from 4 different spheroids were analyzed using the Color Deconvolution Algorithm (using Version 9 default parameters). The brown pixels (positive pixels) were identified as weak, medium, and strong, and reported as percentage out of total brown positive pixels detected. The values reported for each condition are the average of the sum of medium and strong pixel percentage and the error is the standard deviation. OriginPro 9.1 was used for data plotting.

### Optical microscopy imaging.

To determine spheroid size and morphology, 10 spheroids of each cell type were imaged every 24 h, starting from day 1 (the day following the seeding of cells) and until day 12 using Zeiss Observer Z1 Axio Microscope with 10x objective. The spheroid diameter was analyzed and plotted using OriginPro 9.1. For spheroid morphology, spheroids were fixed at day 12 of culture and imaged. 2D cultures were imaged at 10x objective. Image processing with ImageJ software[39] included brightness, contrast, and levels adjustment. Image processing was done consistently across all conditions.

Author Manuscript Author Manuscript Author Manuscript Author Manuscript

### nanoCT imaging.

For the nanoCT analysis, 6 spheroids were imaged, 2 for each cell type.

Fixed spheroids were washed with PBS and DI water, and were stained with iodine[40]. The samples were stained by adding 0.5 mL DI water followed by 150 μL Lugol's EMS solution (1% $I_2$, 2% KI, Electron Microscopy Sciences) for 30 minutes. The spheroids were washed with DI water, transferred to 0.5 mL centrifuge tubes and mounted in 2% low melt agarose solution in the bottom of the tube. The scans were performed on a Zeiss Versa 520 CT. Each scan was performed at 60kV and 5W. Tomographic data was reconstructed from 1601 fluoroscopy images taken with a 20 second exposure time, at a resolution of 0.4–0.5 microns per pixel (no binning at camera or during reconstruction). The data was binned to a final resolution of 0.8–0.9 microns/pixel.

### 3D nanoCT Image analysis.

Analysis of the nanoCT data was carried out on the image stack using Avizo® Fire to visualize the spheroid morphology and the particles within the spheroid in 3D. The data set was cropped and the spheroid organic structure, pores and bright particles were segmented based on their difference in density using the threshold, magic wand and brush tools. The spheroid volume was volume rendered. For estimating the spheroid volume, as well as the volume fraction of the particles and pores in the spheroid, the segmented volume was compared by applying the Volume Fraction tool on the segmentation labels, generating a label voxel count for each feature. For particle characterization, 14 particles were observed in MCF10DCIS.com spheroids and 40 particles in MCF10CA1a spheroids. Their diameters were measured using Avizo® Fire measurement tool. The presented particle size is the average diameter and the error is the standard deviation. For particle per volume calculation, the volume of spheroids in which the particles were observed was calculated by applying the Volume Fraction tool on their segmented labels. Using Avizo, an inner volume, corresponding to the core, of radius 100 μm for the DCIS spheroids and 137 μm for the invasive spheroids, was defined. We then counted particles within that inner volume and compared that number to particles within an outer spherical shell.

### Scanning Electron Microscopy and EDS.

The cryo sections were carbon coated and analyzed in a Mira3 FESEM (Tescan, Czech Republic). High resolution images were acquired at 5 keV at working distance 3 mm with the in-beam secondary electron detector and the in-beam backscatter detector. EDS was carried out at 10 keV at working distance 15 mm using Bruker EDS detector. For SEM imaging and EDS analysis, EDS maps were acquired from at least three regions within 3 spheroid sections and a minimum of 5 particles was examined from each region. For each map, the acquisition time was 12 minutes to ensure adequate counts for calcium signal. The Esprit EDS software was used to generate maps and analyze EDS data and OriginPro 9.1 was used for data plotting. Count intensities were normalized based on the Ca peak intensity.

### Synchrotron XRF and XANES analyses.

20 μm-thick sections of spheroids mounted on Kapton tape were mapped for XRF elemental distributions and microbeam XANES was acquired for regions of interest. Measurements

Author Manuscript Author Manuscript Author Manuscript Author Manuscript

were carried out in Brookhaven National Laboratory (BNL) National Synchrotron Light Source II (NSLS II) in the 8-BM Tender Energy X-ray Absorption Spectroscopy (TES) beamline. Si(111) monochromator and Helium sample environment were used. For elemental XRF mapping, the samples were raster-scanned with dwell time of 2 s per pixel and a step size of 3.125 μm at 4200 eV. All shown data were measured using the same calibration. The emitted fluorescence signal was detected by Ge and Si-drift solid-state fluorescence detectors. For XANES measurements, the X-ray beam energy was continuously scanned from 3976 to 4136 eV with 0.3 eV energy step size, and beam size of 6 × 3 μm. For each point, 80 scans (24 s each) were acquired. As a reference standard, XANES of synthetic hydroxyapatite was measured[41]. Four sections from different spheroids were mapped using XRF. For each spheroid section, XANES was acquired for 4 calcium-rich particles. Analysis was made using Athena software package[42], in which the 80 spectra were merged, and the merged spectra were background-subtracted and edge-step normalized.

## Results

We ask the question of how are cancer cells involved in MC formation in breast tumors – via a cell-mediated regulated process, an out-of-balance dysregulated process, or an unregulated, dystrophic crystallization associated with dead or dying cells? Also, if MC formation is cell-mediated, how does it vary as a function of malignancy potential of the cells and is it related to a physiological process such as bone mineralization?

As most MCs form within the 3D microenvironment of mammary ducts, multicellular spheroid models were used for this study to recapitulate physiologically relevant culture context *in vitro*. Since DCIS is the breast cancer subtype most commonly associated with MCs[43], immortalized human breast epithelial cells that induce the development of ductal carcinoma *in vivo* (MCF10DCIS.com) were cultured in 3D for extended periods of times (>10 days). These culture times allow the spheroids to reach and maintain diameters larger than 300 μm, in which regions of low cell density with dead and dying cells developed at the core due to limited diffusion of oxygen and nutrients. To ensure physiological relevance of the model, we cultured the spheroids in media that contained calcium, magnesium, and phosphate concentrations similar to human blood, and lacked any osteogenic additives (see Supplementary Table 1 for comparison of media composition to typical DMEM/F12 culture media). As a control, cell-free wells with the same media content and conditions were examined under optical microscope and verified that mineral deposition did not occur from solution in the absence of cells.

Spheroids of DCIS cells were spherical in shape and, past a certain culture time (approximately 5 days), were too dense to allow light propagation, rendering them opaque using light microscopy (Fig. 1a, Supplementary Fig. S1). Spheroid diameter growth rate appeared linear up to 12 days (Fig. 1a) and, with increased culture time, the core became notably larger and darker (Supplementary Fig. S1). To better understand the spheroid 3D structure and image both their core and periphery, we utilized nano-computed tomography (nanoCT), generating high resolution data sets with pixel sizes of approximately 500 nm. Fig. 1b shows low cell density at the core of the spheroid, as well as the presence of bright

Author Manuscript Author Manuscript Author Manuscript Author Manuscript

particles. Fig. 1c shows nanoCT 2D slices of the 3D volume of the spheroid, while the fine surface morphology of the spheroid can be seen in Fig. 1d. The 3D interior view reveals that the spheroid, which looks homogenous and spherical using light microscopy, contains multiple lumens. To gain further information regarding the cellular arrangement within the DCIS spheroid model and to confirm that it recapitulated histopathological features of DCIS in clinical samples, we compared hematoxylin & eosin (H&E)-stained histological cross-sections from both the DCIS spheroid model and actual patient samples. Consistent with the nanoCT images, the spheroids contain a core region with lower cell density and regions of cell death, surrounded by a viable cell region around the periphery (Fig. 1e and Supplementary Fig. S2a,c). The clinical DCIS specimen (Fig. 1f) presented similar lumen-like morphologies and areas of lower nuclear density that could be related to either cell death or reminiscent secretory functions of mammary epithelial cells.

The bright particles observed in the spheroid (Fig. 1b) are of dense material and may indicate the presence of mineral particles. Attempts to visualize phosphate mineral particles using von Kossa staining of spheroid sections showed very few, if any, particles that stained brown (Supplementary Fig. S3). To further look for evidence of mineral particles, we examined thin sections of frozen spheroids using scanning electron microscopy (SEM). Unlike standard procedures, we did not wash away the cryoprotectant embedding material (OCT, see Methods), thus maintaining small mineral particles that may be lost during conventional staining methods involving multiple washing steps, such as the von Kossa staining. Similar to our observations from nanoCT scans and H&E-stained histological cross-sections, the resulting cryosections contained cellular material and many lumens in the spheroid interior (Fig. 2a). Higher magnification secondary and back-scattered electron imaging of the spheroid section reveal that high-density particles are embedded inside the matrix, many of them of sub-micron diameter (Fig. 2 b–c). Energy dispersive X-ray spectroscopy (EDS) elemental analysis of the high-density particles showed that the particles contain calcium, phosphorus, and sulfur (Fig. 2c). These calcium-containing particles are observed in both the core and the periphery of the spheroid section. EDS elemental analysis of other areas of the same sample, in which back-scattered electron signal was not observed, did not contain calcium (Supplementary Fig. S4).

To study the mineral distribution in the spheroid sections and to determine the mineral phase, we used synchrotron-based X-ray fluorescence (XRF) and X-ray absorption-near-edge-structure (XANES) analyses of unwashed thin sections. Unlike bulk crystal characterization methods in which it is challenging to detect small mineral particles within large amounts of organic material, this synchrotron-based method allows us to first localize mineral particles within the section by using XRF element mapping, and directly obtain information about their local atomic structure through XANES analysis[44–46]. XRF maps of the sections show that sulfur and phosphorus are dispersed within the tissue, while calcium is localized into dense particles (Fig. 2 d, Supplementary Fig. S5). Some of the calcium-rich particles also presented high phosphorus signal, from which Ca K-edge XANES was acquired (Supplementary Fig. S5 a). The XANES spectra (Fig. 2e) of calcium- and phosphorus-rich particles suggest that the particles are composed of substituted (or non-stoichiometric) apatite, and possibly also sulfur-containing mineral. In comparison to the Ca K-edge XANES spectrum of synthetic hydroxyapatite nanoparticles, the pre-edge 1s-3d

Author Manuscript Author Manuscript Author Manuscript Author Manuscript

peak location (4047.2 eV) of the particles is the same, while the peak intensity of hydroxyapatite is slightly higher. The edge shoulder (1s-4s transition) is clear for hydroxyapatite at 4052.4 eV, while less pronounced for the particles. Both the particles and hydroxyapatite show an energy split at the white line energy (4055.4 eV - 4058.4 eV, 1s-4p transitions) and their peaks are similar in intensity. The XANES of the particles shows a peak at 4062.9 eV, which is present in calcium phosphates, and corresponds to 5s-unoccupied state transitions[47]. The high intensity of the 4062.9 eV peak relative to the hydroxyapatite standard may also be attributed to the presence of calcium sulphate[48].

To better understand whether the malignant potential of breast cancer cells influences MC formation, we expanded our experiment to include not only the MCF10DCIS.com (ductal carcinoma in situ) cells, but also the MCF10A (benign) and MCF10CA1a (invasive) mammary epithelial cells. Mineral formation across the tumor progression series was first evaluated in 2D culture, without the addition of osteogenic additives to the culture media (Supplementary Fig. S6). As the malignancy potential of the cells increased, both Alizarin red staining (ARS) and von Kossa staining increased, indicating an increase in mineral formation consistent with previous results[24]. Moving into 3D culture, spheroids of the non-malignant and invasive cells were characterized using light microscopy and nanoCT (Fig. 3 a–d) and differed in their morphology and sizes (Supplementary Fig. S7). Interestingly, the invasive spheroids show a similar linear growth rate to the DCIS, while the non-malignant spheroids actually decrease in size with time (Supplementary Fig. S7A). Much like the DCIS spheroids, the invasive spheroids were spherical and dense, showing a dark core through which light does not propagate, while the non-malignant cell spheroid core was less dense. The fine surface morphology of the spheroids, as imaged with the nanoCT, showed that the non-malignant breast cells form less spherical structures than the more invasive cells in the tumor progression series (Fig. 3 c, d). The more spherical shapes of the spheroids formed by the malignant cells may be related to the increased contractile forces of these cells relative to their less malignant counterparts. H&E-stained histological cross-sections of the spheroids clearly showed the lack of a necrotic core in the non-malignant MCF10A spheroids (Fig. 3e). In contrast, both the DCIS and invasive spheroids developed distinct cores in which regions of dying cells with low cell density and of necrosis were separated from the viable cell regions located at the spheroid periphery (Fig. 1e, Fig. 3f, Supplementary Fig. S2). Von Kossa staining of these spheroid sections showed very few, if any, particles that stained brown, and only in the pre-cancer and invasive spheroids (Supplementary Fig. S3).

XRF imaging confirmed the presence of calcium phosphate particles in the invasive spheroids, similar to those found in the DCIS spheroids (Supplementary Fig. S8). The Ca-edge XANES spectra from these particles were very similar to those obtained for the particles formed in the DCIS spheroids (Fig. 2e), suggesting that the mineral phase within the invasive spheroids is also a substituted, non-stoichiometric apatite (Supplementary Fig. S8).

After showing that both DCIS and CA1a spheroids were associated with MCs, while they were absent in MCF10A spheroids, we next used nanoCT to localize, in 3D, the mineral particles in the different areas of the spheroids. Dense particles were observed in the nanoCT

Author Manuscript Author Manuscript Author Manuscript Author Manuscript

scans as bright granules, compared to the gray color of the cells and matrix, which were stained with iodine for contrast enhancement. For the non-malignant cells, almost no particles were observed in the spheroids. In comparison, for the DCIS and invasive spheroids, multiple bright particles were clearly observed (Fig. 4 a,b). By using the brightness difference, the dense particles were segmented from the nanoCT data and were represented as red particles dispersed in the spheroid volume (Fig. 4 a,d, Supplementary video S9). The particle diameters detected in the DCIS and invasive spheroids ranged from sub-micron to approximately 20 μm, while the average particle size in the DCIS and invasive spheroids was 7±3 μm and 11±5 μm, respectively. The number of particles in the DCIS and invasive spheroids per volume of $10^7$ $\mu m^3$ is 1.8 and 2.6, respectively (Fig. 4 b,e). Due to resolution limits, however, the nanoCT data does not represent the actual particle distribution in the spheroid and excludes sub-micron particles, which are known to exist in the spheroids based upon SEM images (Fig. 2).

Even with that caveat, the nanoCT data does suggest that there is a difference between the DCIS and invasive spheroids: there are more, and larger, particles dispersed in the spheroid volume of the invasive spheroids as compared to the DCIS spheroids. Finally, the core was identified by the nanoCT as a separate area at the spheroid center, which had lower contrast and defined visible boundaries. For the DCIS spheroids, this core was ~ 100 μm in radius, while for the invasive spheroids it was ~ 140 μm. Interestingly, for both DCIS and invasive spheroids, almost all particles were detected outside of the core, in the viable cell area (Fig. 4 c,f). In the DCIS spheroids, 30% of the particles were found within the 100 μm radius core, while 70% were found within a spherical shell with an inner radius of 100 μm and an outer radius of 150 μm. In the invasive spheroids, no particles were detected within the inner core and 100% of the particles were found within a spherical shell with an inner radius of 137 μm and an outer radius of 212 μm.

To better understand what, if any, cellular regulation is contributing to MC formation, immunohistochemistry of spheroid cross-sections was used to detect proteins with known roles in regulating mineralization: Alkaline phosphatase (ALP) and Osteopontin (OPN). ALP is an early osteoblast marker expressed by osteoblasts during bone mineralization, which converts pyrophosphates into free inorganic phosphate, thus acting as a promoter of mineralization[49]. OPN is a protein strongly affecting mineralization, most often as an inhibitor [50–52], which is also highly expressed in breast cancer[21,53] and is associated with MCs[19,54].

Immunohistochemical analysis of sections stained for ALP shows high intensity staining of the non-malignant spheroids, a prominent yet weaker staining of the DCIS spheroids, and a very low intensity of the invasive spheroids (Fig. 5, top left). The trend was opposite for OPN immunohistochemistry, in which the non-malignant spheroids showed very low staining, which increased in the DCIS spheroids and was the strongest in the invasive spheroids (Fig. 5, top right). These results were further confirmed by image analysis of the immune-stained sections. Taken together, these results suggest that ALP levels decrease with increasing spheroid malignancy and mineral particle number and size, while OPN levels increase with increasing malignancy and mineral particle number and size (Fig. 5 bottom).

Author Manuscript Author Manuscript Author Manuscript Author Manuscript

## Discussion

Mineral particles were observed mostly in the viable cell area of the spheroids and not in the cores that consist of dead and dying cells, and the particle sizes and number increased with malignancy: non-malignant < DCIS < invasive. Hence, MC deposition directly correlated with spheroid malignancy potential. This trend, combined with the observation that most of the particles were located in the viable cell area and not in areas of necrosis, shows that in this 3D breast tumor model, cancer cells produce MCs in an active manner, even without exogeneous induction of osteogenic differentiation. In addition, our findings indicate that increased MC formation in the spheroids corresponds to upregulation of OPN and downregulation of ALP, which could suggest mineral formation due to an imbalance of mineralization inhibitors and promotors that is dependent on the cell malignancy potential. Taken together, these findings suggest that in the spheroid breast tumor model, the mechanism for MC formation is a combination of dysregulated (imbalance of mineralization inhibitors and promotors) and unregulated (necrosis-related) processes, but is distinct from a cellularly regulated, physiological bone-like process (Fig. 6).

2D cultures served as a comparison for the 3D spheroids, and were used to evaluate the relationship between cell phenotype and mineralization ability. The non-malignant cells showed minor staining of both alizarin red (calcium detection) and von Kossa (phosphate-mineral detection), while the staining intensity of both stains increased with malignancy: non-malignant < DCIS < invasive (Supplementary Fig. S6). Alizarin red and von Kossa staining of MCF10DCIS.com and MCF10CA1a showed relatively homogeneous mineral deposition, unlike the isolated patches observed in the spheroids. When considering the observed increase in mineral deposition with increasing cell malignancy, two scenarios come to mind: One is that the more invasive cells have an increased tendency to mineralization, and the second is that the more invasive cultures contain higher amounts of cell debris that may serve as nucleation site and induce unregulated mineralization. In 2D cultures, we cannot distinguish between these two pathways.

The 3D spheroid model allowed us to differentiate between mineralization processes related to cell death and to viable cells. As described, the nanoCT data provided evidence that in the 3D spheroids, more MCs are associated with the viable cell region than with the core. Our SEM data (Fig. 2a–c) and previous results[15], however, showed that mineralization also occurs in core areas, both *in vitro* and in tissues. MCs in the core most likely form by unregulated mineralization[56–59], but possibly via a dysregulated process followed by cell death. Without further time-resolved observations, we cannot differentiate between these two possibilities.

Using high resolution imaging, synchrotron XRF mapping, and XANES, we identified apatite particles formed in both types of the malignant spheroids. As it is known that human MCs are either calcium oxalate[55,60] or calcium phosphate minerals[1,2,15,59,61–63], the fact that the spheroids reported here can produce non-stoichiometric apatite, the most common calcium phosphate mineral found in breast tissues, shows the relevance of this model to MC mechanistic studies. Future studies comparing Ca-edge and P-edge XANES of the mineral particles found in the spheroids to microcalcifications from human tissue

Author Manuscript Author Manuscript Author Manuscript Author Manuscript

samples may further inform the relevance of the model. The mineralized particle sizes reported here ranged from sub-micron to 20 μm, below the resolution limit of mammography. Similar sizes of MCs were recently reported in human breast tumor tissue samples and could represent early stages of mineralization that then grow to the larger sizes detected by mammography[15]. 3D localization of sub-micron particles within the spheroids, however, will require the use of higher resolution volume techniques, such as Focused Ion Beam-Scanning Electron Microscopy imaging[64,65].

The occurrence of the key mineralization proteins OPN and ALP inside the spheroids was assessed using immunostaining. OPN levels increased with spheroid malignancy and MC number, supporting the recently suggested connection between OPN upregulation and MC formation[66]. OPN is generally regarded as a mineralization inhibitor[67–70] that regulates mineralization in a manner dependent on its phosphorylation state[71,72]. Importantly, in addition to breast MCs[19–21], OPN is often found associated with pathological mineral deposits such as kidney stones[73] and calcifications of papillary thyroid carcinoma[74]. The occurrence of OPN with pathological mineral deposits in vivo suggests that OPN might either be involved in the deposition of mineral or, more consistent with its role as an inhibitor, be upregulated in response to abnormal mineral deposition. Further research is clearly required to better understand the complex role of OPN in MC formation pathways. In contrast to OPN levels, ALP levels were high in the spheroids formed by non-malignant and DCIS cells, and these levels decreased in the spheroids formed by invasive cells, which also contain the largest number of mineral particles. This trend suggests that elevated ALP levels are not directly related to elevated mineralization in the spheroids. Interestingly, 2D culture of the same non-malignant cell line used here in 3D, showed low levels of ALP[24]. As ALP is associated with physiological mineralization, it is less likely that MC mineralization is a bone-like mechanism, as was recently suggested in *in vitro* studies of 2D cultures[3,24,25]. Also, collagen, which has a crucial role in regulated physiological mineralization and comprises up to 60% of bones, was demonstrated to not be associated with MCs *in vivo*[14,59].

## Conclusions

3D multicellular spheroids recapitulating different stages of breast cancer progression can serve as an *in vitro* model for studying MC formation mechanisms. Without osteogenic additives and in the presence of culture media that contains physiological concentrations of calcium, mineralization increases with spheroid malignancy potential, is associated with increased OPN and decreased ALP levels, and occurs primarily in the viable cell area of the spheroids. This model demonstrates an active role for breast cancer cells in MC formation, however, the observed mineralization is different from cellularly regulated physiological mineralization and is suggested to be the result of a combination of cellularly dysregulated and unregulated processes.

By providing a physiologically relevant culture microenvironment that is amenable to further modification, e.g., by incorporating additional stromal cell types, varying the ECM context, or applying varied soluble factor gradients, the described model system can be used to identify which other parameters present in breast cancer patients, but lacking in conventional

Author Manuscript Author Manuscript Author Manuscript Author Manuscript

2D culture models may be affecting MC formation. Furthermore, the spheroid model can be extended to more in depth mechanistic studies of MC formation, including tracking the transport of calcium and phosphate ions within the spheroid, analyzing the 3D distribution of particles smaller than the detection limit of conventional methods, testing inhibitors of certain mineralization proteins, and exploring the relation between MCs, cancer metabolism, and therapy response. Beyond investigations of MC formation pathways, this spheroid model has the potential to provide insights into other aspects of breast cancer pathology. For example, further studies can characterize changes in the composition of the extracellular matrix as a function of malignancy potential (e.g., lipid and protein content), explore the origins of the lumen-like morphologies, and observe cellular changes as a function of culture time. Taken together, the results from this study contribute to our understanding of the link between MC formation and tumor pathogenesis and will inform future studies of MCs within human breast tumors.

## Supplementary Material

Refer to Web version on PubMed Central for supplementary material.

## Acknowledgements

We thank the Cornell College of Veterinary Medicine Animal Health Diagnostic Center staff and for the use of Scanscope, the Schaffer-Nishimura lab for use of the cryotome. The human DCIS sample was provided by Drs. Clifford A. Hudis and Neil M. Iyengar of the Memorial Sloan Kettering Cancer Center. Synchrotron experiments were carried out at Brookhaven National Laboratory (BNL) National Synchrotron Light Source II (NSLS II), a user facility supported under Contract No. DE-SC0012704; Beamline 8-BM was funded in part by NASA (NNX13AD12G), NSF (EAR-1128957) and DOE (DE-FG02–12ER16342). We thank Prof. Pupa Gilbert and Dr. Kenneth Finkelstein for discussion of XANES data, Mr. Jooho Kim for XANES hydroxyapatite standard and Dr. Siyoung Choi for helpful discussions. We thank Dr. Daniel Sudilovsky of the Department of Pathology and Laboratory Medicine, Cayuga Medical Center at Ithaca for his pathological expertise. Research reported in this publication was supported by the National Cancer Institute of the National Institutes of Health under award number R01CA173083, the Center on the Physics of Cancer Metabolism through Award Number 1U54CA210184-01, and by the Human Science Frontiers Program (RGP0016/2017). The content is solely the responsibility of the authors and does not necessarily represent the official views of the National Institutes of Health. This work made use of the Cornell Center for Materials Research Shared Facilities which are supported through the NSF MRSEC program (DMR-1719875). Additional imaging data was acquired through the Cornell University Biotechnology Resource Center, with NIH 1S10OD012287 funding. N.V. acknowledges funding from The Israeli Council for Higher Education and Ben-Gurion University.

## References

[1]. Baker R, Rogers KD, Shepherd N, Stone N, New relationships between breast microcalcifications and cancer, Br. J. Cancer 103 (2010) 1034–1039. [PubMed: 20842116]

[2]. Haka AS, Shafer-Peltier KE, Fitzmaurice M, Crowe J, Dasari RR, Feld MS, Identifying microcalcifications in benign and malignant breast lesions by probing differences in their chemical composition using Raman spectroscopy, Cancer Res 62 (2002) 5375–5380. [PubMed: 12235010]

[3]. Scimeca M, Giannini E, Antonacci C, Pistolese CA, Spagnoli LG, Bonanno E, Microcalcifications in breast cancer: an active phenomenon mediated by epithelial cells with mesenchymal characteristics, BMC Cancer. 14 (2014) 286. [PubMed: 24758513]

[4]. Wang Z, Hauser N, Singer G, Trippel M, Kubik-Huch RA, Schneider CW, Stampanoni M, Non-invasive classification of microcalcifications with phase-contrast X-ray mammography, Nat. Commun 5 (2014) 3797. [PubMed: 24827387]

Author Manuscript Author Manuscript Author Manuscript Author Manuscript

[5]. Rimer JD, An Z, Zhu Z, Lee MH, Goldfarb DS, Wesson JA, Ward MD, Crystal growth inhibitors for the prevention of L-cystine kidney stones through molecular design, Science. 330 (2010) 337–341. [PubMed: 20947757]

[6]. Luo G, Ducy P, McKee MD, Pinero GJ, Loyer E, Behringer RR, Karsenty G, Spontaneous calcification of arteries and cartilage in mice lacking matrix GLA protein, Nature. 386 (1997) 78–81. [PubMed: 9052783]

[7]. Bertazzo S, Gentleman E, Cloyd KL, Chester AH, Yacoub MH, Stevens MM, Nano-analytical electron microscopy reveals fundamental insights into human cardiovascular tissue calcification, Nat. Mater 12 (2013) 576–583. [PubMed: 23603848]

[8]. Hutcheson JD, Goettsch C, Bertazzo S, Maldonado N, Ruiz JL, Goh W, Yabusaki K, Faits T, Bouten C, Franck G, Quillard T, Libby P, Aikawa M, Weinbaum S, Aikawa E, Genesis and growth of extracellular-vesicle-derived microcalcification in atherosclerotic plaques, Nat. Mater 15 (2016) 335–343. [PubMed: 26752654]

[9]. Reznikov N, Steele JAM, Fratzl P, Stevens MM, A materials science vision of extracellular matrix mineralization, Nat. Rev. Mater 1 (2016) 16041.

[10]. Varsano N, Fargion I, Wolf SG, Leiserowitz L, Addadi L, Formation of 3D cholesterol crystals from 2D nucleation sites in lipid bilayer membranes: Implications for atherosclerosis, J. Am. Chem. Soc 137 (2015) 1601–1607. [PubMed: 25584426]

[11]. Varsano N, Dadosh T, Kapishnikov S, Pereiro E, Shimoni E, Jin X, Kruth HS, Leiserowitz L, Addadi L, Development of correlative cryo-soft X-ray tomography and stochastic reconstruction microscopy. A study of cholesterol crystal early formation in cells, J. Am. Chem. Soc 138 (2016) 14931–14940. [PubMed: 27934213]

[12]. Farmanesh S, Chung J, Sosa RD, Kwak JH, Karande P, Rimer JD, Natural promoters of calcium oxalate monohydrate crystallization, J. Am. Chem. Soc 136 (2014) 12648–12657. [PubMed: 25119124]

[13]. Weiner S, Addadi L, Crystallization pathways in biomineralization, Annu. Rev. Mater. Res 41 (2011) 21–40.

[14]. Kumar V, Abbas AK, Aster JC, Robbins And Cotran Pathologic Basis Of Disease, 9th ed., Saunders, Philadelphia, PA, 2014.

[15]. Kunitake JAMR, Choi S, Nguyen KX, Lee MM, He F, Sudilovsky D, Morris PG, Jochelson MS, Hudis CA, Muller DA, Fratzl P, Fischbach C, Masic A, Estroff LA, Correlative imaging reveals physiochemical heterogeneity of microcalcifications in human breast carcinomas, J. Struct. Biol 202 (2018) 25–34. [PubMed: 29221896]

[16]. Ghadially FN, As you like it, Part 3: A critique and historical review of calcification as seen with the electron microscope, Ultrastruct. Pathol 25 (2001) 243–67.

[17]. Kim KM, Apoptosis and calcification, Scanning Microsc 9 (1995) 1137–78. [PubMed: 8819895]

[18]. Majno G, Joris I, Cells, Tissues, and Disease, 2nd ed., Oxford University Press, New York, 2004.

[19]. Oyama T, Sano T, Hikino T, Xue Q, Iijima K, Nakajima T, Koerner F, Microcalcifications of breast cancer and atypical cystic lobules associated with infiltration of foam cells expressing osteopontin, Virchows Arch 440 (2002) 267–273. [PubMed: 11889596]

[20]. Bellahcène A, Merville M-P, Castronovo V, Bellahcã A, Merville M-P, Castronovo V, Expression of Bone Sialoprotein, a bone matrix protein, in human breast cancer, Cancer Res 54 (1994) 2823–2826. [PubMed: 8187059]

[21]. Bellahcène A, Castronovo V, Increased expression of osteonectin and osteopontin, two bone matrix proteins, in human breast cancer, Am. J. Pathol 146 (1995) 95–100. [PubMed: 7856741]

[22]. Scimeca M, Antonacci C, Toschi N, Giannini E, Bonfiglio R, Buonomo CO, Pistolese CA, Tarantino U, Bonanno E, Breast Osteoblast-like cells a reliable early marker for bone metastases from breast cancer, Clin. Breast Cancer. S1526–8209 (2017) 30209–4.

[23]. Jahnen-Dechent W, Heiss A, Schäfer C, Ketteler M, Fetuin-A regulation of calcified matrix metabolism, Circ. Res 108 (2011) 1494–509. [PubMed: 21659653]

[24]. Cox RF, Hernandez-Santana A, Ramdass S, McMahon G, Harmey JH, Morgan MP, Microcalcifications in breast cancer: novel insights into the molecular mechanism and functional consequence of mammary mineralisation, Br. J. Cancer 106 (2012) 525–37. [PubMed: 22233923]

Author Manuscript Author Manuscript Author Manuscript Author Manuscript

[25]. Cox RF, Morgan MP, Microcalcifications in breast cancer: Lessons from physiological mineralization, Bone. 53 (2013) 437–450. [PubMed: 23334083]

[26]. Leboy PS, Vaias L, Uschmann B, Golub E, Adams SL, Pacifici M, Ascorbic acid induces alkaline phosphatase, type X collagen, and calcium deposition in cultured chick chondrocytes, J. Biol. Chem 264 (1989) 17281–6. [PubMed: 2793855]

[27]. Wan X-C, Liu C-P, Li M, Hong D, Li D-M, Chen H-X, Li J-C, Staphylococcal enterotoxin C injection in combination with ascorbic acid promotes the differentiation of bone marrow-derived mesenchymal stem cells into osteoblasts in vitro, Biochem. Biophys. Res. Commun 373 (2008) 488–492. [PubMed: 18572015]

[28]. Boskey AL, Roy R, Cell culture systems for studies of bone and tooth mineralization, Chem. Rev 108 (2008) 4716–4733. [PubMed: 18800815]

[29]. Fischbach C, Chen R, Matsumoto T, Schmelzle T, Brugge JS, Polverini PJ, Mooney DJ, Engineering tumors with 3D scaffolds, Nat. Methods 4 (2007) 855–860. [PubMed: 17767164]

[30]. Seo BR, DelNero P, Fischbach C, In vitro models of tumor vessels and matrix: Engineering approaches to investigate transport limitations and drug delivery in cancer, Adv. Drug Deliv. Rev 69–70 (2014) 205–216.

[31]. Infanger DW, Lynch ME, Fischbach C, Engineered culture models for studies of tumor-microenvironment interactions, Annu. Rev. Biomed. Eng 15 (2013) 29–53. [PubMed: 23642249]

[32]. Bin Kim J, Stein R, O'Hare MJ, Three-dimensional in vitro tissue culture models of breast cancer — a review, Breast Cancer Res. Treat 85 (2004) 281–291. [PubMed: 15111767]

[33]. Yuhas JM, Li AP, Martinez AO, Ladman AJ, A simplified method for production and growth of multicellular tumor spheroids, Cancer Res 37 (1977) 3639–364. [PubMed: 908012]

[34]. Maguire SL, Peck B, Wai PT, Campbell J, Barker H, Gulati A, Daley F, Vyse S, Huang P, Lord CJ, Farnie G, Brennan K, Natrajan R, Three-dimensional modelling identifies novel genetic dependencies associated with breast cancer progression in the isogenic MCF10 model, J. Pathol 240 (2016) 315–328. [PubMed: 27512948]

[35]. Soule HD, Maloney TM, Wolman SR, Peterson WD, Brenz R, McGrath CM, Russo J, Pauley RJ, Jones RF, Brooks SC, Isolation and characterization of a spontaneously immortalized human breast epithelial cell line, MCF-10, Cancer Res 50 (1990) 6075–86. [PubMed: 1975513]

[36]. Miller FR, Santner SJ, Tait L, Dawson PJ, MCF10DCIS.com xenograft model of human comedo ductal carcinoma in situ, J. Natl. Cancer Inst 92 (2000) 1185–6.

[37]. Barnabas N, Cohen D, Phenotypic and molecular characterization of MCF10DCIS and SUM breast cancer cell lines, Int. J. Breast Cancer. 2013 (2013) 872743. [PubMed: 23401782]

[38]. Santner SJ, Dawson PJ, Tait L, Soule HD, Eliason J, Mohamed AN, Wolman SR, Heppner GH, Miller FR, Malignant MCF10CA1 cell lines derived from premalignant human breast epithelial MCF10AT cells, Breast Cancer Res. Treat 65 (2001) 101–110. [PubMed: 11261825]

[39]. Schneider CA, Rasband WS, Eliceiri KW, NIH Image to ImageJ: 25 years of image analysis, Nat. Methods 9 (2012) 671–675. [PubMed: 22930834]

[40]. Metscher BD, MicroCT for comparative morphology: simple staining methods allow high-contrast 3D imaging of diverse non-mineralized animal tissues, BMC Physiol 9 (2009) 11–25. [PubMed: 19545439]

[41]. Pathi SP, Lin DDW, Dorvee JR, Estroff LA, Fischbach C, Hydroxyapatite nanoparticle-containing scaffolds for the study of breast cancer bone metastasis, Biomaterials. 32 (2011) 5112–5122. [PubMed: 21507478]

[42]. Ravel B, Newville M, IUCr ATHENA, ARTEMIS HEPHAESTUS: data analysis for X-ray absorption spectroscopy using IFEFFIT, J. Synchrotron Radiat 12 (2005) 537–541. [PubMed: 15968136]

[43]. Hofvind S, Iversen BF, Eriksen L, Styr BM, Kjellevold K, Kurz KD, Mammographic morphology and distribution of calcifications in ductal carcinoma in situ diagnosed in organized screening, Acta Radiol 52 (2011) 481–487. [PubMed: 21498306]

[44]. Politi Y, Levi-Kalisman Y, Raz S, Wilt F, Addadi L, Weiner S, Sagi I, Structural characterization of the transient amorphous calcium carbonate precursor phase in sea urchin embryos, Adv. Funct. Mater 16 (2006) 1289–1298.

Author Manuscript Author Manuscript Author Manuscript Author Manuscript

[45]. Krejci MR, Wasserman B, Finney L, McNulty I, Legnini D, Vogt S, Joester D, Selectivity in biomineralization of barium and strontium, J. Struct. Biol 176 (2011) 192–202. [PubMed: 21871966]

[46]. Politi Y, Metzler RA, Abrecht M, Gilbert B, Wilt FH, Sagi I, Addadi L, Weiner S, Gilbert PUPA, Gilbert P, Transformation mechanism of amorphous calcium carbonate into calcite in the sea urchin larval spicule, Proc. Natl. Acad. Sci. U. S. A 105 (2008) 17362–6. [PubMed: 18987314]

[47]. Eichert D, Salomé M, Banu M, Susini J, Rey C, Preliminary characterization of calcium chemical environment in apatitic and non-apatitic calcium phosphates of biological interest by X-ray absorption spectroscopy, Spectrochim. Acta - Part B At. Spectrosc 60 (2005) 850–858.

[48]. Pascolo L, Gianoncelli A, Rizzardi C, Tisato V, Salomé M, Calligaro C, Salvi F, Paterson D, Zamboni P, Calcium micro-depositions in jugular truncular venous malformations revealed by Synchrotron-based XRF imaging, Sci. Rep 4 (2014) 1–10.

[49]. Millán JL, Alkaline phosphatases Structure, substrate specificity and functional relatedness to other members of a large superfamily of enzymes, Purinergic Signal. 2 (2006) 335–341. [PubMed: 18404473]

[50]. Boskey AL, Maresca M, Ullrich W, Doty SB, Butler WT, Prince CW, Osteopontin-hydroxyapatite interactions in vitro: inhibition of hydroxyapatite formation and growth in a gelatin-gel, Bone Miner 22 (1993) 147–159. [PubMed: 8251766]

[51]. McKee MD, Nanci A, Osteopontin at mineralized tissue interfaces in bone, teeth, and osseointegrated implants: Ultrastructural distribution and implications for mineralized tissue formation, turnover, and repair, Microsc. Res. Tech 33 (1996) 141–164. [PubMed: 8845514]

[52]. McKee MD, Nanci A, Osteopontin: an interfacial extracellular matrix protein in mineralized tissues, Connect Tissue Res 35 (1996).

[53]. Brown LF, Papadopoulos-Sergiou A, Berse B, Manseau EJ, Tognazzi K, Perruzzi CA, Dvorak HF, Senger DR, Osteopontin expression and distribution in human carcinomas, Am. J. Pathol 145 (1994) 610–23. [PubMed: 8080043]

[54]. Wang X, Chao L, Chen L, Jin G, Hua M, Liu H, Ouyang A, Zhang X, Primary breast carcinoma: Association of mammographic calcifications with osteopontin, Radiology. 254 (2010) 69–78. [PubMed: 20019131]

[55]. Busing CM, Keppler U, Menges V, Differences in microcalcification in breast tumors, Virchows Arch. A Pathol. Anat. Histol 393 (1981) 307–313.

[56]. Hoda SA, Brogi E, Koerner FC, Rosen PP, Rosen's Breast Pathology, Fourth edi, Lippincott Williams & Wilkins, Philadelphia, 2014.

[57]. Evans A, Pinder S, Wilson R, Sibbering M, Poller D, Elston C, Ellis I, Ductal carcinoma in situ of the breast: correlation between mammographic and pathologic findings, Am. J. Roentgenol 162 (1994) 1307–1311. [PubMed: 8191988]

[58]. Leborgne R, Diagnosis of tumors of the breast by simple roentgenography; calcifications in carcinomas, Am. J. Roentgenol. Radium Ther 65 (1951) 1–11.

[59]. Hassler O, Microradiographic investigations of calcifications of the female breast, Cancer. 23 (1969) 1103–9. [PubMed: 4305104]

[60]. Radi MJ, Calcium oxalate crystals in breast biopsies. An overlooked form of microcalcification associated with benign breast disease, Arch. Pathol. Lab. Med 113 (1989) 1367–9. [PubMed: 2589947]

[61]. Frappart L, Boudeulle M, Boumendil J, Lin HC, Martinon I, Palayer C, Mallet-Guy Y, Raudrant D, Bremond A, Rochet Y, Feroldi J, Structure and composition of microcalcifications in benign and malignant lesions of the breast: Study by light microscopy, transmission and scanning electron microscopy, microprobe analysis, and X-ray diffraction, Hum. Pathol 15 (1984) 880–889.

[62]. Ahmed A, Calcification in human breast carcinomas: Ultrastructural observations, J. Pathol 117 (1975) 247–251. [PubMed: 1214193]

[63]. Scott R, Stone N, Kendall C, Geraki K, Rogers K, Relationships between pathology and crystal structure in breast calcifications: an in situ X-ray diffraction study in histological sections, NPJ Breast Cancer. 2 (2016) 16029. [PubMed: 28721386]

Author Manuscript Author Manuscript Author Manuscript Author Manuscript

[64]. Schertel A, Snaidero N, Han H-M, Ruhwedel T, Laue M, Grabenbauer M, Möbius W, Cryo FIB-SEM: Volume imaging of cellular ultrastructure in native frozen specimens, J. Struct. Biol 184 (2013) 355–360. [PubMed: 24121039]

[65]. Vidavsky N, Akiva A, Kaplan-Ashiri I, Rechav K, Addadi L, Weiner S, Schertel A, Cryo-FIB-SEM serial milling and block face imaging: Large volume structural analysis of biological tissues preserved close to their native state, J. Struct. Biol 196 (2016) 487–495. [PubMed: 27693309]

[66]. Cross BM, Breitwieser GE, Reinhardt TA, Rao R, Cellular calcium dynamics in lactation and breast cancer: from physiology to pathology, AJP Cell Physiol 306 (2014) C515–C526.

[67]. Boskey AL, Spevak L, Paschalis E, Doty SB, McKee MD, Osteopontin deficiency increases mineral content and mineral crystallinity in mouse bone, Calcif. Tissue Int 71 (2002) 145–154. [PubMed: 12073157]

[68]. Giachelli CM, Steitz S, Osteopontin: a versatile regulator of inflammation and biomineralization, Matrix Biol 19 (2000) 615–622. [PubMed: 11102750]

[69]. Steitz SA, Speer MY, McKee MD, Liaw L, Almeida M, Yang H, Giachelli CM, Osteopontin inhibits mineral deposition and promotes regression of ectopic calcification, Am. J. Pathol 161 (2002) 2053–2046. [PubMed: 12466122]

[70]. Speer MY, McKee MD, Guldberg RE, Liaw L, Yang H-Y, Tung E, Karsenty G, Giachelli CM, Inactivation of the osteopontin gene enhances vascular calcification of matrix Gla protein–deficient mice, J. Exp. Med 196 (2002) 1047–1055. [PubMed: 12391016]

[71]. Gericke A, Qin C, Spevak L, Fujimoto Y, Butler WT, Sørensen ES, Boskey AL, Importance of phosphorylation for osteopontin regulation of biomineralization, Calcif. Tissue Int 77 (2005) 45–54. [PubMed: 16007483]

[72]. Jono S, Peinado C, Giachelli CM, Phosphorylation of osteopontin is required for inhibition of vascular smooth muscle cell calcification, J. Biol. Chem 275 (2000) 20197–20203. [PubMed: 10766759]

[73]. Mazzali M, Kipari T, Ophascharoensuk V, Wesson JA, Johnson R, Hughes J, Osteopontin—a molecule for all seasons, QJM An Int. J. Med 95 (2002) 3–13.

[74]. Wu G, Guo J-J, Ma Z-Y, Wang J, Zhou Z-W, Wang Y, Correlation between calcification and bone sialoprotein and osteopontin in papillary thyroid carcinoma, Int. J. Clin. Exp. Pathol 8 (2015) 2010–7. [PubMed: 25973097]

Author Manuscript Author Manuscript Author Manuscript Author Manuscript

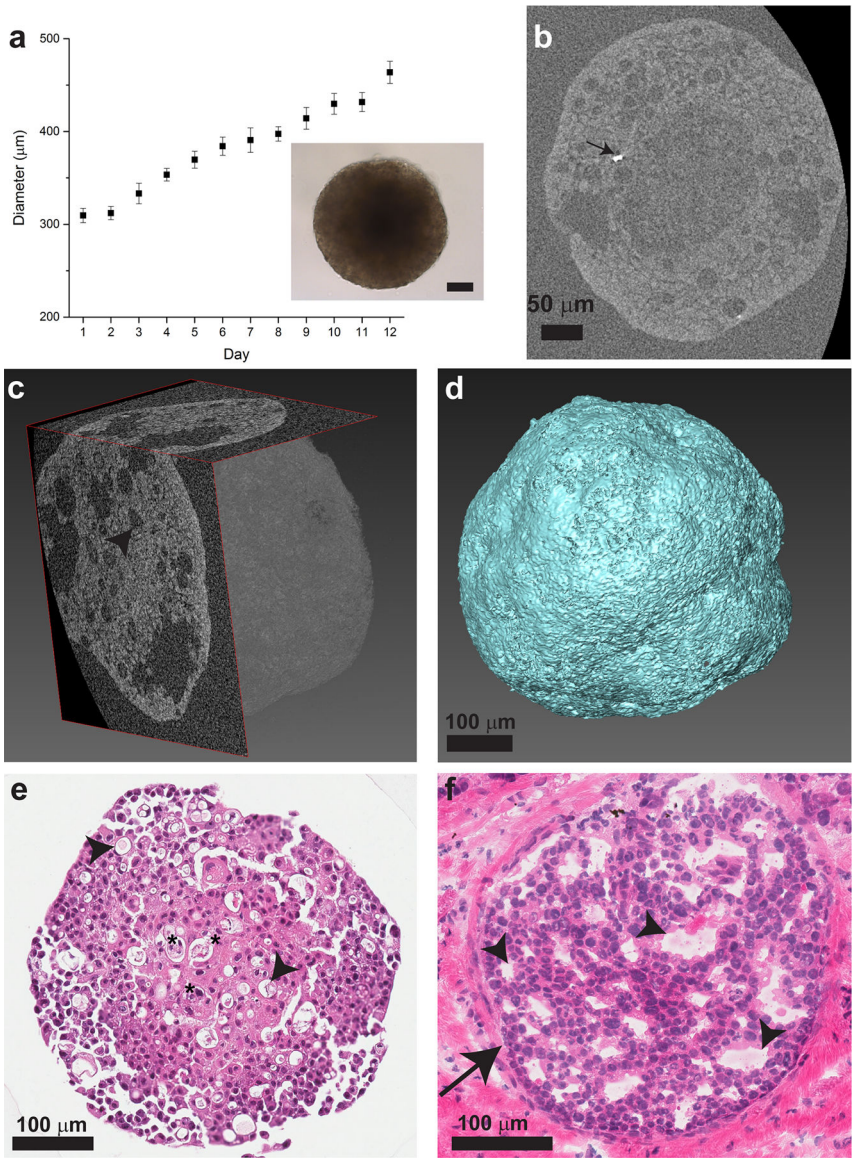


**Fig. 1.**

DCIS spheroid characterization. **a:** Spheroid diameter dependence on time, $n = 10$ spheroids with standard deviation as the error bars. Inset: Light microscope image of a spheroid, scale bar: 50 μm. **b:** 2D slice of the spheroids from nanoCT data, showing the low cell density core in the center. Dense particles (arrow) are brighter than the organic matrix (stained with iodine to increase the contrast of the organic matrix) (Day 13). **c:** 3D reconstruction of a spheroid from nanoCT scan data showing two orthogonal 2D slices of the spheroid and its generated volume. **d:** 3D volume of reconstructed and segmented nanoCT data showing spheroid surface morphology. **e:** H&E staining of a spheroid cross section showing cell nuclei in purple and cytoplasm in pink (Day 12). Regions of cell death are located at the core (stars). **f:** H&E staining of clinical sample of human breast ductal carcinoma in situ (arrow) and surrounding tissue. **c, e, f:** Lumens presenting as a decrease in cell density are observed

Author Manuscript Author Manuscript Author Manuscript Author Manuscript

(arrowheads). See Supplementary Fig. S2 for higher magnification images of H&E staining of the core and periphery of DCIS spheroids.

Author Manuscript Author Manuscript Author Manuscript Author Manuscript

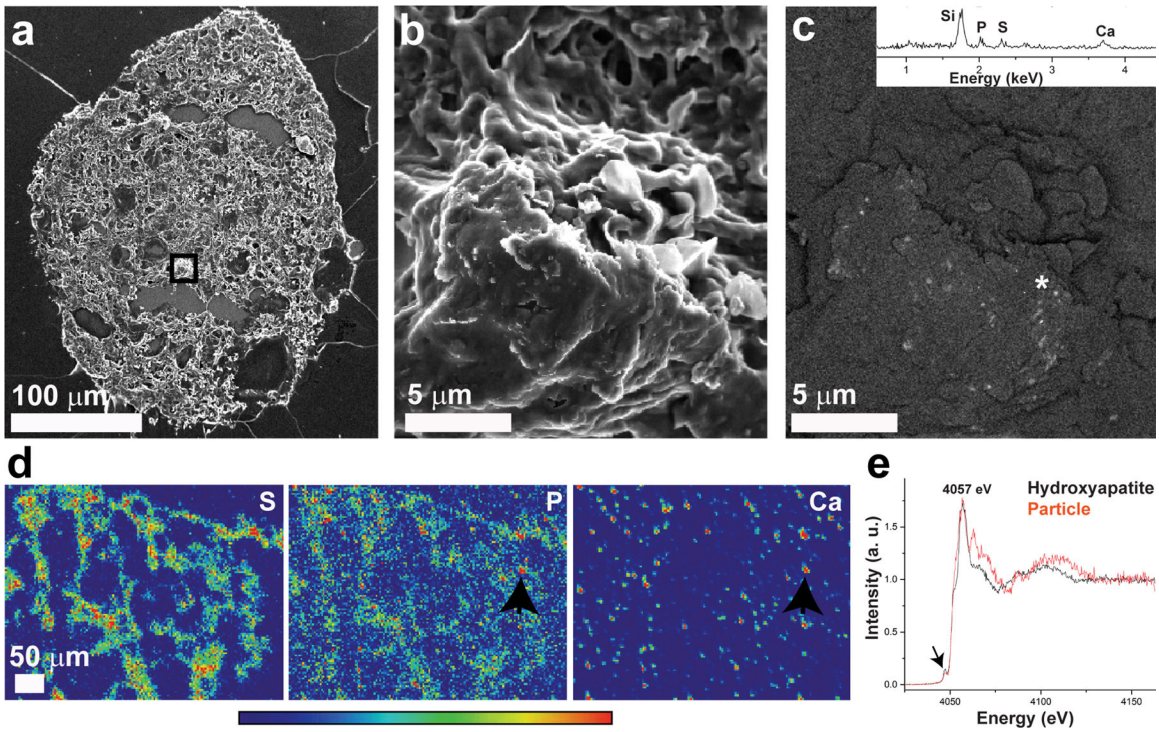


**Fig 2.**

Mineralized particles in pre-cancer DCIS.com spheroids. **a:** Scanning electron micrograph of secondary electron signal of a spheroid section in which the marked area is magnified in b-c. **b:** Scanning electron micrograph of secondary electron signal showing a magnification of the core area marked in (a), showing the spheroid tissue structure**. c:** Scanning electron micrograph of back-scattered electron signal from the same areas as (b) showing sub-micron bright particles of high density embedded in the tissue. **Inset:** EDS spectrum obtained from the bright particles area marked with an asterisk, showing presence of calcium, phosphorus and sulfur. Note that the silicon signal results from the quartz slide substrate. **d:** XRF maps of a spheroid section showing sulfur (S), phosphorus (P) and calcium (Ca) distribution. The sulfur distribution mostly overlaps with the section shape, as sulfur is a typical element found in biological tissues. Phosphorus is also abundant in the section in a dispersed manner, while calcium is more localized in “hot spots”. The XANES spectrum of a particle in which strong calcium and phosphorus signals are overlapping (arrows) is shown in (e). **e:** Ca K-edge XANES of the particle marked in (d) and a hydroxyapatite standard, both measured under the same conditions. Peak assignments are based on Eichert et al[47], note global 5 eV energy shifts from our data. The pre-edge is marked with an arrow.

Author Manuscript Author Manuscript Author Manuscript Author Manuscript

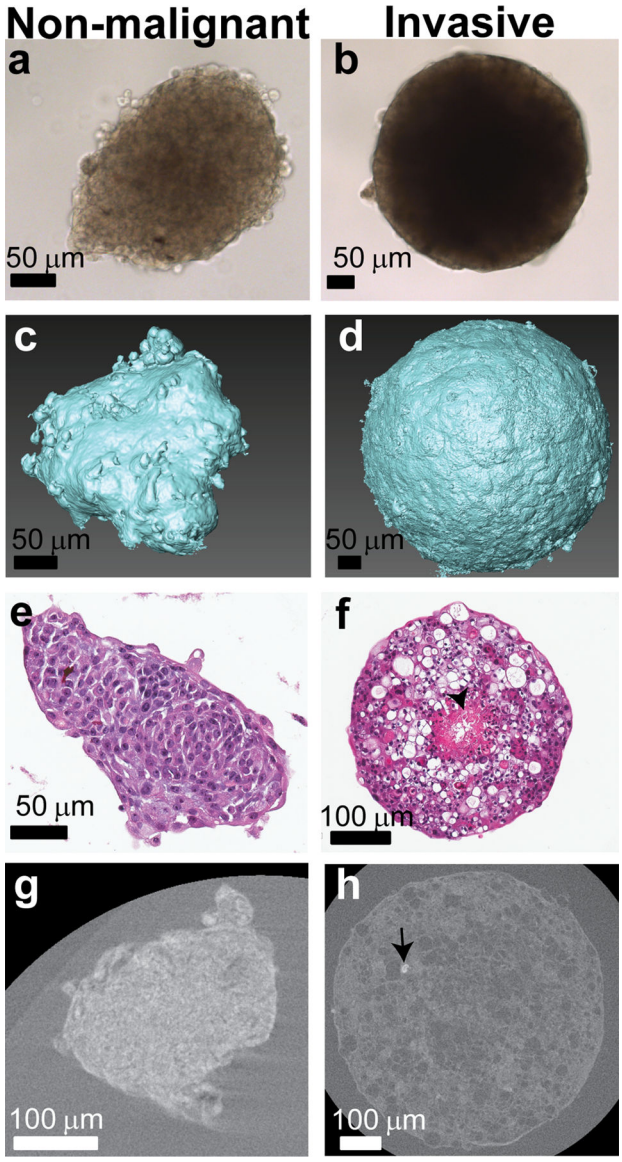


**Fig. 3.**

Characterization of non-malignant MCF10A (day 13) (a, c, e, g) and invasive MCF10CA1a (day 12) (b, d, f, h) spheroids. **a, b:** Light microscope images of MCF10A (a) and MCF10Ca1a (b) spheroids. **c, d:** 3D volumes of the reconstructed and segmented MCF10A (c) and MCF10Ca1a (f) spheroids showing their surface morphology. **e, f:** H&E stained histological cross-sections of MCF10A (c) and MCF10CA1a (d) spheroids. **g, h:** 2D slices of MCF10A (g) and MCF10CA1a (h) spheroids from nanoCT data (stained with iodine to increase the contrast of the organic matrix), showing the spheroid cross section and bright particle within the MCF10CA1a (arrow). No particles are observed in the MCF10A spheroids. See Supplementary Fig. S2 for higher magnification images of H&E staining of the core and periphery of MCF10CA1a spheroids.

Author Manuscript Author Manuscript Author Manuscript Author Manuscript

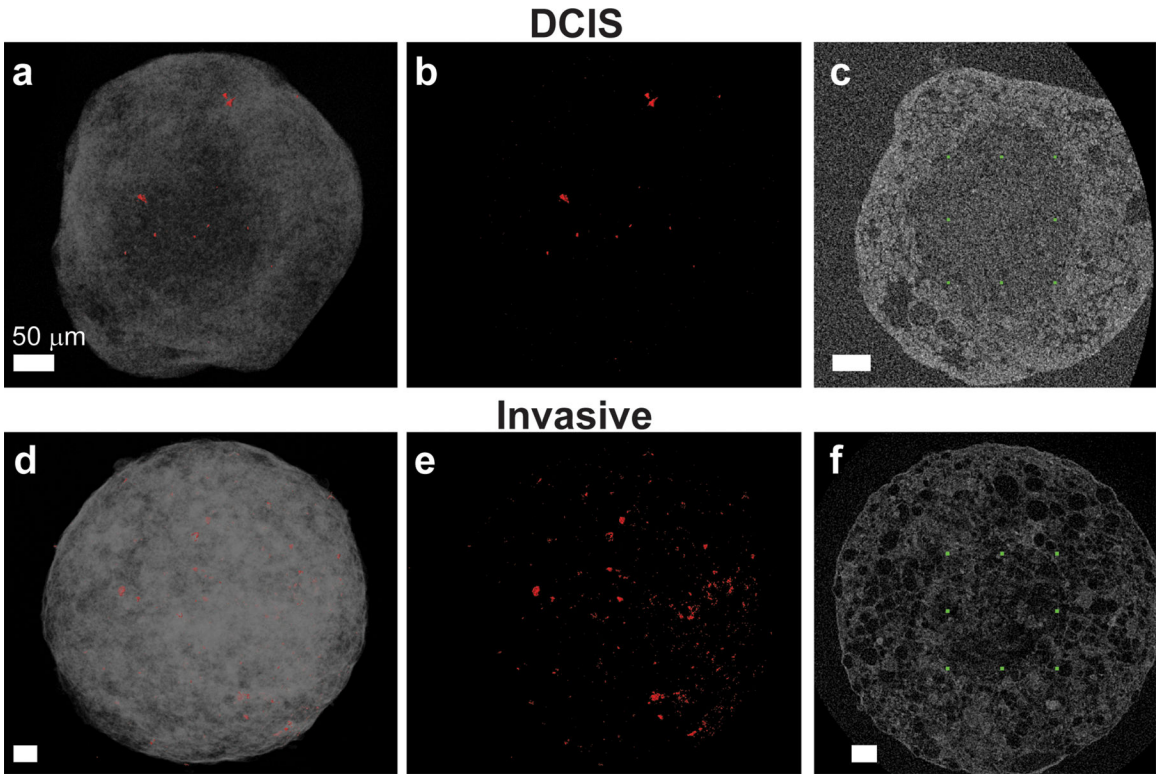


**Fig 4.**

NanoCT reconstructed data showing MCF10DCIS.com (a-c) and invasive MCF10CA1a (d-f) spheroids, stained with iodine to increase the contrast of the organic matrix. **a, d:** Volume rendering of the spheroid volume is shown in gray. High-density particles are shown in red and are visible close to the spheroid surface. **b, e:** The bright particles of higher density were segmented from the 3D scans and are presented in red, shown throughout the entire spheroid volume. **c, f:** Identification of the "core areas". The rectangle outlined by green symbols is a 2D representation of a cube whose entire volume is enclosed within the core. Bright particles that are observed inside this volume are considered as located in the core. In both cell types, the majority of the high-density particles are localized outside the spheroid cores. Supplementary video S9 provides 3D reconstruction of the spheroid slices, as well as particle segmentation. All scale bars are 50 μm.

Author Manuscript Author Manuscript Author Manuscript Author Manuscript

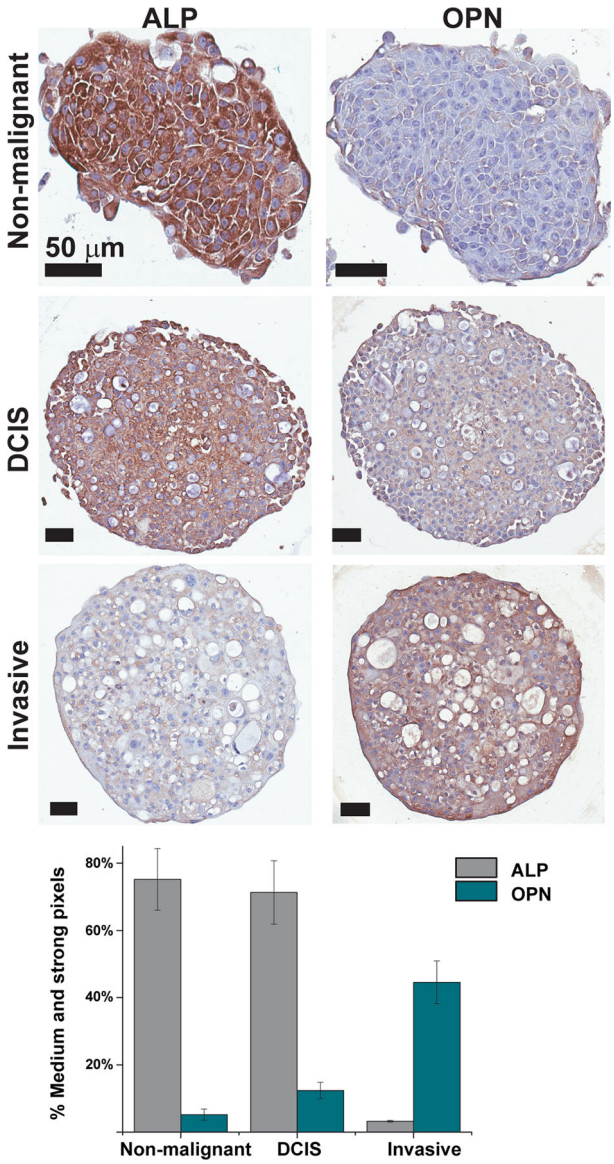


**Fig.5.**

Top: Immunohistochenistry of the non-malignant, in situ carcinoma and invasive spheroid cross sections, showing the protein staining (brown) and counter-stain (blue) for alkaline phosphotase (ALP) and osteopontin (OPN) (Day 12). Bottom: Image analysis of immunostained cross-sections showing percentage of strong and medium positive (brown) pixels out of total positive pixels for ALP and OPN stained spheroid sections. Error bars represent standard deviations.

Author Manuscript Author Manuscript Author Manuscript Author Manuscript

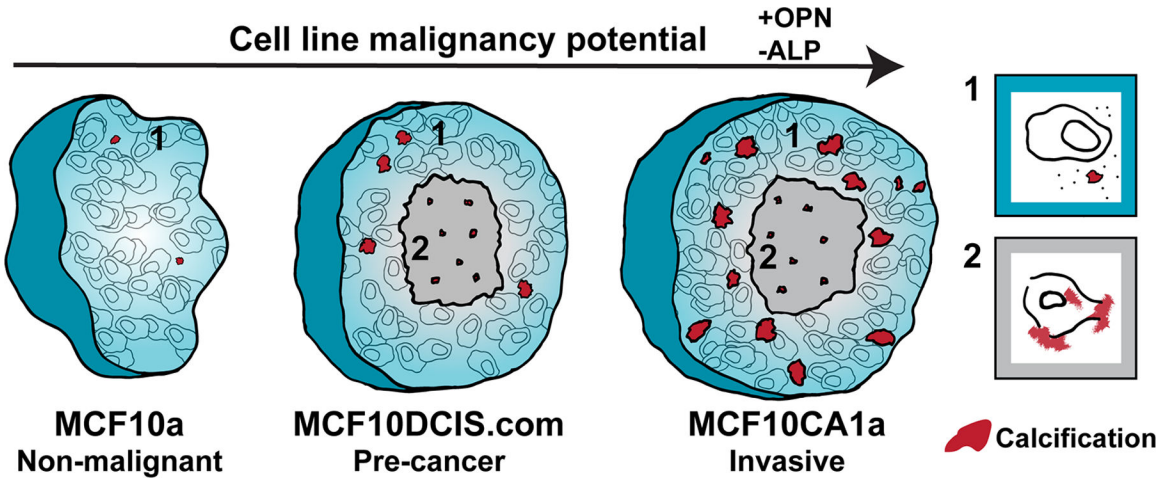


**Fig 6.**

A schematic description of the proposed mineralization pathways in the 3D in vitro breast cancer model of multicellular spheroids. Osteopontin (OPN) expression levels increase and alkaline phosphatase (ALP) expression levels decrease with an increase of cell line malignancy potential. Viable cell area (1) is shown in cyan and the necrotic core (2) is shown in gray. Calcification is shown in red. The non-malignant spheroids show no necrotic core and almost no calcifications are formed. With an increase of malignancy from non-malignant to pre-cancer to invasive, the number of calcifications increases. In both pre-cancer and invasive spheroids, more calcifications form in the viable cells area than in the necrotic core, and the calcifications formed in the core are smaller. In the necrotic areas, calcification formation is similar for both pre-cancer and invasive spheroids. Possible scenerios for mineral deposition by cells in each area are shown to the right: (1) cellularly dysregulated calcification, involving, for example, an imbalance of protein inhibitors and promoters of calcification (2) unregulated calcification, involving mineral formation in areas of cell death.